Measurements of the ground-state polarizabilities of Cs, Rb, and K using atom interferometry

Maxwell D. Gregoire,[1] Ivan Hromada,[1] William F. Holmgren,[1] Raisa Trubko,[2] and Alexander D. Cronin[1,2,*]

[1]*Department of Physics, University of Arizona, Tucson, Arizona 85721, USA*
[2]*College of Optical Sciences, University of Arizona, Tucson, Arizona 85721, USA*

We measured the ground-state static electric-dipole polarizabilities of Cs, Rb, and K atoms using a three-nanograting Mach-Zehnder atom beam interferometer. Our measurements provide benchmark tests for atomic structure calculations and thus test the underlying theory used to interpret atomic parity-nonconservation experiments. We measured $\alpha_{\rm Cs} = 4\pi\epsilon_0 \times 59.39(9)\,{\rm \mathring{A}}^3$, $\alpha_{\rm Rb} = 4\pi\epsilon_0 \times 47.39(8)\,{\rm \mathring{A}}^3$, and $\alpha_{\rm K} = 4\pi\epsilon_0 \times 42.93(7)\,{\rm \mathring{A}}^3$. In atomic units, these measurements are $\alpha_{\rm Cs} = 401.2(7)$, $\alpha_{\rm Rb} = 320.1(6)$, and $\alpha_{\rm K} = 290.0(5)$. We report ratios of polarizabilities $\alpha_{\rm Cs}/\alpha_{\rm Rb} = 1.2532(10)$, $\alpha_{\rm Cs}/\alpha_{\rm K} = 1.3834(9)$, and $\alpha_{\rm Rb}/\alpha_{\rm K} = 1.1040(9)$ with smaller fractional uncertainty because the systematic errors for individual measurements are largely correlated. Since Cs atom beams have short de Broglie wavelengths, we developed measurement methods that do not require resolved atom diffraction. Specifically, we used phase choppers to measure atomic beam velocity distributions, and we used electric field gradients to give the atom interference pattern a phase shift that depends on atomic polarizability.

I. INTRODUCTION

Measurements of static electric-dipole polarizabilities serve as benchmark tests for *ab initio* calculations of electric-dipole transition-matrix elements. These calculations require understanding quantum many-body systems with relativistic corrections, and there are many different methods that attempt to calculate these matrix elements in a reasonable amount of computing time [1]. Testing these methods is important because these matrix elements are used to calculate several atomic properties, such as lifetimes, oscillator strengths, line strengths, van der Waals interaction potentials and associated cross sections, Feshbach resonances, and photoassociation rates. Measuring alkali-metal static polarizabilities as a means of testing atomic structure calculations has been of interest to the physics community since Stark's pioneering measurements in 1934 [2]. Static polarizabilities have been measured using deflection [2–5], an E-H gradient balance [6,7], times of flight of an atomic fountain [8], and phase shifts in atomic and molecular interferometers [9–12].

We measured the static electric-dipole polarizabilities of K, Rb, and Cs atoms with 0.16% uncertainty using a Mach-Zehnder three-grating atom interferometer [13,14] with an electric field gradient interaction region. We used the same apparatus for all three elements, so we can also report polarizability ratios with 0.08% uncertainty because the sources of systematic uncertainty are largely correlated between our measurements of different atoms' polarizabilities.

We compare our measurements to *ab initio* calculations of atomic polarizabilities and to polarizabilities deduced from studies of atomic lifetimes, Feshbach resonances, and photoassociation spectroscopy. We also use our measurements to report the Cs $6p_{1/2}$ and $6p_{3/2}$ state lifetimes, Rb $5p_{1/2}$ and $5p_{3/2}$ state lifetimes, and K $4p_{1/2}$ and $4p_{3/2}$ state lifetimes and the associated principal electric-dipole matrix elements, oscillator strengths, and line strengths. Then we use our measurements to report van der Waals C_6 coefficients, and we

combine our measurements with measurements of transition Stark shifts to report some excited-state polarizabilities with better than 0.09% uncertainty.

Testing Cs atomic structure calculations by measuring $\alpha_{\rm Cs}$ is valuable for atomic parity-nonconservation (PNC) research, which places constraints on beyond-the-standard-model physics. The PNC amplitude $E_{\rm PNC}$ due to Z^0-mediated interactions between the Cs valence electron and the neutrons in its nucleus can be written in terms of electric-dipole transition-matrix elements and the nuclear weak-charge parameter Q_W. Atomic structure calculations are needed to deduce a value of Q_W from an $E_{\rm PNC}$ measurement [15–18] to compare to the Q_W predicted by the standard model [19,20]. Our measurement of $\alpha_{\rm Cs}$ tests the methods used to calculate the relevant matrix elements and provides a benchmark for the $\langle 6s_{1/2} \| \hat{D} \| 6p_{1/2} \rangle$ matrix element, one of the terms in the expression for $E_{\rm PNC}$.

Here we report atom interferometry measurements of Cs, Rb, and K polarizability that have smaller fractional uncertainty than the pioneering sodium polarizability measurement by Ekstrom *et al.* in 1995 [9]. Because it is challenging to resolve Cs atomic diffraction—our nanogratings diffract our Cs atom beams with only 20 μrad between diffraction orders—we designed an experiment with an electric field gradient instead of a septum electrode, such as was used in [9,10]. We also developed phase choppers [22–25] to measure our atom beams' velocity distributions instead of using atom diffraction to study velocity distributions, as was done in [9,11]. These two innovations enable us to measure polarizabilities of heavy atoms such as Cs without resolving diffraction patterns. Without the need to resolve diffraction, we can use larger collimating slits and a wider detector to obtain data more quickly. These innovations also reduce some systematic errors that are related to beam-alignment imperfections.

We improved the accuracy of our measurements compared to our previous work [11] by redesigning the electrodes that apply phase shifts to our interferometer. This configuration of electrodes, i.e., two parallel, oppositely charged cylindrical pillars, allows us to determine the distance between the atom
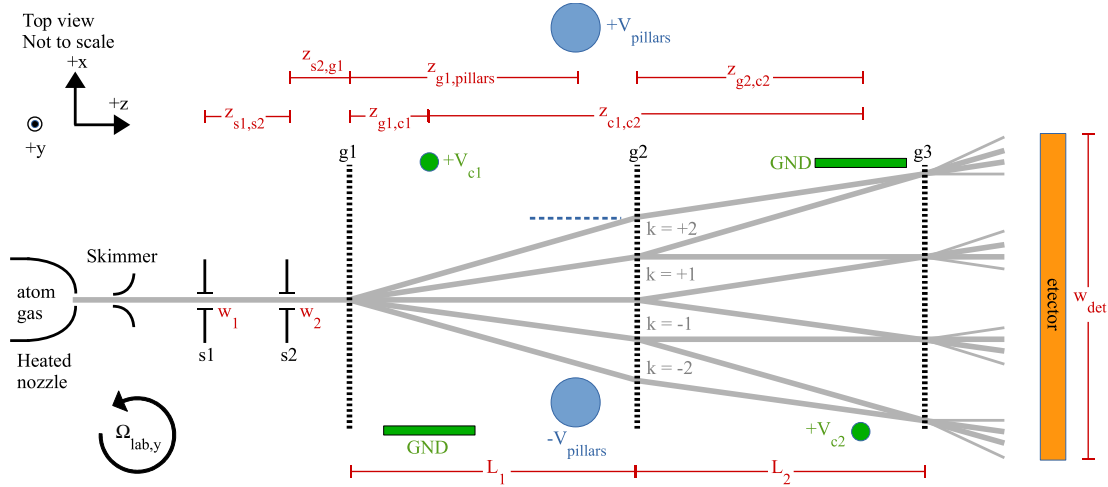
---

*cronin@physics.arizona.edu

FIG. 1. (Color online) Diagram of the Mach-Zehnder atom interferometry apparatus with phase choppers (green) and electrodes that produce an electric field gradient (blue). Dimensions are shown in red and tabulated in Table I. The supersonic atom beam, shown in gray, is collimated by two slits, s1 and s2, with widths w_1 and w_2 before entering the first grating. The nanogratings, g1, g2, and g3, are spaced longitudinally such that $L_1 = L_2$, which causes an interference pattern to form at the position of g3. We consider the four separate interferometers in our data analysis, labeled with $k = +2, +1, -1, -2$, that form via zeroth-, $\pm$first-, and $\pm$second-order diffraction from g1. The atoms are detected by a platinum Langmuir-Taylor detector [21], indicated in orange. The pair of blue circles represents oppositely charged cylindrical electrodes (extending perpendicular to the page) that form a virtual ground plane between them. The electric field from these electrodes polarizes the atoms and thereby shifts the interference pattern's phase. The phase choppers are shown in green; each phase chopper is a charged wire next to a grounded plane. The geometry terms relevant to the pillars and phase choppers are displayed in Fig. 2 and discussed in Sec. II A. Due to the rotation of the Earth, the laboratory has a rotation rate about the vertical axis of $\Omega_{\text{lab},y} = 38.88\ \mu\text{rad/s}$ that is also relevant to our analysis.

beam and the virtual ground plane between the pillars with reduced statistical uncertainty. We reduced systematic error by making more accurate measurements of the width of the gap between the pillars, the pillars' radii, the voltages on the pillars, and the distance between the pillars and the first diffraction grating. Our measurements also required a sophisticated model of the apparatus, which included interference formed by the zeroth, $\pm$first, and $\pm$second diffraction orders, the finite thickness and divergence of the beam, and the finite width of the detector [25]. Because beams of Cs, Rb, and K had different velocity distributions and diffraction angles, we developed a more detailed error analysis in order to understand how those attributes affected the systematic uncertainties in polarizability measurements of different atoms. To support our error analysis, we also developed a method to monitor and adjust the distances between nanogratings in our interferometer.

II. APPARATUS DESCRIPTION AND ERROR ANALYSIS

A schematic diagram of the three-grating Mach-Zehnder atom beam interferometer we use to make our measurements is shown in Fig. 1. A mixture of He and Ar gas carries Cs, Rb, or K vapor through a 50 μm nozzle to generate a supersonic atom beam [26,27]. We adjust the carrier gas composition to change the beam's average velocity: a higher percentage of Ar results in a slower beam. The atom beam passes through two collimating slits and diffracts through three silicon nitride nanogratings, each with period $d_g = 99.90(0.5)$ nm [28,29]. The first two gratings manipulate the atoms' de Broglie waves to form a 99.90 nm period interference pattern at the position of the third grating. The method of observing interference fringes is described in detail in [30]: we scan the second grating in the

$\pm x$ direction and observe the flux admitted through the third grating in order to determine the interference pattern's contrast and phase. We measure that transmitted atomic flux with a 100-μm-wide platinum wire Langmuir-Taylor detector [21].

In the rest of Sec. II, we describe how we measure the atoms' velocity distribution and polarizability. We measure v_0, the atoms' mean velocity, using phase choppers, which are charged wires parallel with the y axis held parallel to grounded planes, indicated in green in Fig. 1. We measure static polarizability α with a nonuniform electric field created by two oppositely charged cylindrical pillars parallel with the y axis and indicated in blue in Fig. 1. The pillars' electric field shifts the interference fringe phase by an amount roughly proportional to α/v_0^2. Section II A describes how the electric field geometry of both the phase choppers and the pillars causes a differential phase shift. Section II B describes how we use the phase choppers to measure the velocity distribution, and Sec. II C describes how we use the pillars to measure α. Section II D discusses how we apply our knowledge of the velocity distribution to analyze the polarizability data taken with the pillars.

A. Phase shifts with cylindrical electrodes

Both the pillars and the phase choppers are described by the geometry shown in Fig. 2, and create electric fields given by

$$\vec{E}(x,z) = \frac{\lambda}{2\pi\epsilon_0}\left[\frac{x-b}{(x-b)^2+z^2} - \frac{x+b}{(x+b)^2+z^2}\right]\hat{x}$$

$$+ \left[\frac{z}{(x-b)^2+z^2} - \frac{z}{(x+b)^2+z^2}\right]\hat{z}, \quad (1)$$
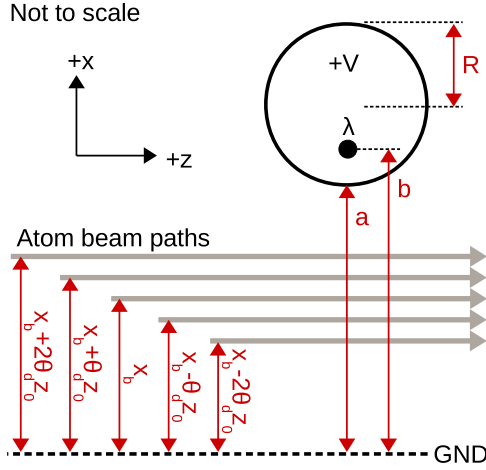
FIG. 2. (Color online) Diagram showing the dimensions, shown in red, that describe the static electric fields created by the pillars and by the phase choppers. The circle represents the cross section of a metal pillar or charged wire with radius R held at voltage V. The GND line represents the ground plane, which may by physical (in the case of the choppers) or virtual (in the case of the pillars). a is the closest distance between the pillar edge and the ground plane. The parameter b is the distance between the ground plane and the effective line charge within the pillar. The atom beam center is a distance x_b away from the ground plane. The different interferometer arms are separated from their neighbors by multiples of $\theta_d z_0$, where θ_d is the diffraction angle and z_0 is the longitudinal distance to grating g1 (in the case of the pillars and chopper c1) or grating g3 (in the case of chopper c2). a and R dimensions for the pillars and phase choppers are given in Table I.

where the effective line charge density

$$\lambda = 2\pi \epsilon_0 V \ln^{-1}\left(\frac{a+R+b}{a+R-b}\right) \tag{2}$$

exists a distance $b = a\sqrt{1 + 2R/a}$ away from the ground plane. The parameter a represents the distance between the ground plane and the closest cylinder edge, R represents the pillars' radius, and the directions $\hat{x}$ and $\hat{z}$ are shown in Fig. 2.

When atoms enter an electric field, their potential energy changes by $U_{\text{Stark}} = -\frac{1}{2}\alpha|\vec{E}|^2$. Since $U_{\text{Stark}} \approx -0.1\ \mu\text{eV}$ and $E_{\text{kinetic}} \approx 1$ eV for Cs in our experiment, we can use the WKB approximation along with the residue theorem to compute the total phase accumulated by an atom traveling through the field. We can also approximate that atoms travel parallel to the ground plane regardless of the angle at which they diffracted and their incident angle upon grating g1. Even though this approximation may be incorrect by up to 10^{-3} rad, such a discrepancy would only cause errors in the accumulated phases by factors of 10^{-6}, which is insignificant for our experiment. Therefore, we represent the accumulated phase along one path for a component of an atomic de Broglie wave as

$$\Phi(v,x) = \frac{1}{\hbar v}\int_{-\infty}^{\infty} \frac{1}{2}\alpha|\vec{E}|^2 dz = \frac{\lambda^2 \alpha}{\pi \epsilon_0^2 \hbar v}\left(\frac{b}{b^2 - x_b^2}\right), \tag{3}$$

where x_b is the distance between the atom's path and the ground plane.

The atoms in our beam form many interferometers, but we only need to consider the four interferometers shown in Fig. 1. Other interferometers are insignificant to our analysis because they have some combination of low contrast and low flux. We label the four interferometers that we do consider with the index $k = +2$, $k = +1$, $k = -1$, and $k = -2$. The differential phase shifts for the four interferometers are

$$\Delta\Phi_{\vec{E},+2}(v,x_b) = \Phi(v,x_b + 2\theta_d z_0) - \Phi(v,x_b + \theta_d z_0),$$
$$\Delta\Phi_{\vec{E},+1}(v,x_b) = \Phi(v,x_b + \theta_d z_0) - \Phi(v,x_b),$$
$$\Delta\Phi_{\vec{E},-1}(v,x_b) = \Phi(v,x_b) - \Phi(v,x_b - \theta_d z_0),$$
$$\Delta\Phi_{\vec{E},-2}(v,x_b) = \Phi(v,x_b - \theta_d z_0) - \Phi(v,x_b - 2\theta_d z_0). \tag{4}$$

In the above equations, $\theta_d z_0$ is the lateral separation between classical paths in the interferometer, where $\theta_d = \lambda_{\text{dB}}/d_g$ is the diffraction angle and z_0 is the distance to the first grating (in the case of the pillars and chopper c1) or the third grating (in the case of chopper c2).

B. Velocity measurement

The atoms in the beam do not all have the same velocity, so the electric fields do not apply the same phase shifts to each diffracted atom. We observe the average phase and contrast of an ensemble of atoms with velocity distribution $P(v)$. We model $P(v)$ as a Gaussian distribution,

$$P(v) = \frac{v_r}{v_0\sqrt{2\pi}}e^{-\frac{v_r^2(v-v_0)^2}{2v_0^2}}, \tag{5}$$

where v_0 is the mean velocity and the velocity ratio $v_r = v_0/\sigma_v$ is a measure of the distribution's sharpness. It is worth noting that the velocity distribution for a supersonic atom beam is better described by a v^3-weighted Gaussian distribution [13]. However, either distribution can be used in our analysis to parametrize the typical high-v_0, high-v_r velocity distributions of our atom beam without changing our polarizability result by more than 0.008%. Since v_0 is the average velocity in a Gaussian but not in a v^3-weighted Gaussian, we use Eq. (5) to simplify our discussion of the error analysis.

To measure v_0 and v_r, we use phase choppers [24,25]. Each phase chopper is a charged wire about 1 mm away from a physical ground plane (see Table I for phase chopper dimensions). Chopper c1 is between the first two gratings and chopper c2 is a distance $z_{c1,c2} = 1269.3 \pm 0.25$ mm downstream of chopper c1, between the last two gratings (see Fig. 1). The voltages on the choppers' wires and the distances between the beam and the choppers' ground planes are chosen such that chopper c1 shifts the ensemble's average phase by $+\pi$ and chopper c2 shifts it by $-\pi$.

When we pulse the choppers on and off at a frequency f_c, an atom may receive a net phase shift of $\pm\pi$ or 0, depending on its velocity and the time at which it passed through the first chopper. Holmgren et al. [24] gives an intuitive explanation of how we measure contrast C vs f_c to determine v_0 and v_r. Figure 3 shows an example of C vs f_c data. Hromada et al. [25] later improved upon Holmgren et al.'s model of C vs f_c by considering how the thickness and divergence of the beam causes some components of the atoms' velocity distribution to not be detected. In the present work, we expanded our

TABLE I. List of apparatus dimensions described in Figs. 1 and 2. Dimensions with no quoted uncertainty have uncertainty much less than what would be significant to our analysis. a_{c1} and a_{c2} are the closest distances between the wires and the ground planes for phase choppers 1 and 2, and $a_{pillars}$ is half the width of the gap between the pillars (the closest distance between the virtual ground plane and either pillar). $L_1 - L_2 = 0 \pm 30$ μm, and the uncertainty in $L_1 + L_2$ is insignificant.

$z_{s1,s2}$	860 mm
$z_{g1,pillars}$	833.5 ± 0.25 mm
$z_{g1,c1}$	269.7 mm
$z_{s2,g1}$	100 mm
$z_{g2,c2}$	598 mm
$z_{c1,c2}$	1269.3 ± 0.25 mm
L_1	940 mm
L_2	940 mm
w_1	30 ± 6 μm
w_2	40 ± 6 μm
w_{det}	100 ± 3 μm
$a_{pillars}$	1999.85 ± 0.5 μm
$R_{pillars}$	6350 ± 0.5 μm
a_{c1}	986 ± 25 μm
R_{c1}	785.5 μm
a_{c2}	893 ± 25 μm
R_{c2}	785.5 μm

analysis to include the four interferometers shown in Fig. 1, performed a more in-depth error analysis, and added an additional calibration step to the measurement procedure, as we discuss next.

Hromada *et al.* described how the thickness and divergence of the beam determine the likelihood for atoms of certain velocities to be detected [25]. The thickness and divergence is defined by the finite widths of the collimating slits w_1 and w_2. The finite width of the detector w_{det} and the detector's offset from the beam line in the x direction Δx_{det} also affect the probability of detecting atoms as a function of the atoms'
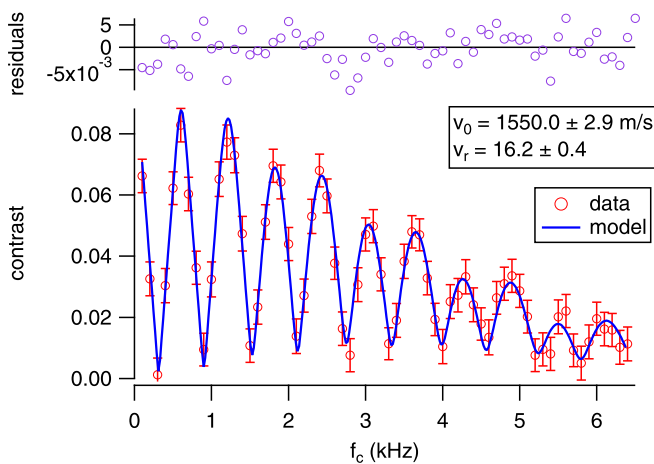

FIG. 3. (Color online) An example of a measurement of contrast C vs phase chopper frequency f_c for a Cs beam. We fit a model to these data that has v_0 and v_r as fit parameters in order to measure the velocity distribution.

velocities and initial positions in the apparatus. The phase and contrast we observe with our detector is that of an ensemble of atoms with different velocities, different incident positions on grating g1, and different incident angles on grating g1.

Uncertainties in w_1, w_2, w_{det}, and Δx_{det} are more significant for beams that are physically wider. In K beams, which have larger θ_d of ≈ 50 μrad and wider velocity distributions ($v_0 \approx 2100$ m/s, $v_r \approx 14$, and therefore $\sigma_v \approx 150$ m/s), more of the lower-velocity atoms in the distribution miss the detector. Therefore, uncertainties in the aforementioned quantities have a higher bearing on how we model the average velocity of detected atoms. Ignoring this component of the analysis would cause a systematic increase in measured v_0 by 0.5% and v_r by 10% for a typical K beam.

Modeling the four interferometers shown in Fig. 1, rather than only the $k = \pm 1$ interferometers, also improved our understanding of how likely it is for certain velocities to be detected. For K beams with wide velocity distributions, we would report v_0 too high by about 0.5% and v_r too low by about 5% if we included only the $k = \pm 1$ interferometers. This is because, for such beams, a much higher proportion of atoms in the $k = \pm 2$ interferometers misses the detector than in the $k = \pm 1$ interferometers. Ignoring the $k = \pm 2$ interferometers has a significant effect on the model of the detected $P(v)$ when the detected velocity distributions for the $k = \pm 1$ and $k = \pm 2$ interferometers are significantly different. Conversely, for Cs and Rb beams, we found no significant difference in results between models because most of the atoms in all interferometers were detected regardless of velocity.

Hromada *et al.* [25] also described how inequality between intergrating distances L_1 and L_2 (see Fig. 1) causes systematic errors. When $\Delta L = L_2 - L_1$ is nonzero, the interference fringes formed at the third grating become magnified or demagnified. We summarize this geometric magnification with the separation phase shift,

$$\Delta \Phi_{sep,k} = \frac{2\pi}{d_g} \left(\theta_{inc} + \frac{k}{2} \theta_d \right) \Delta L, \tag{6}$$

where k is the interferometer index (see Fig. 1) and θ_{inc} is the incident angle on grating g1. To reduce systematic error in our v_0 and v_r measurements, we measure ΔL and set it equal to zero.

Equation (6) implies that uncertainty in ΔL is more significant for beams with larger θ_d, such as K beams. Also, because $\Delta \Phi_{sep,k}$ has a component proportional to θ_{inc}, uncertainty in ΔL is more significant for more divergent beams. As $|\Delta L|$ increases, uncertainties in w_1, w_2, w_{det}, and Δx_{det} become more significant. Accordingly, we developed a method to set $\Delta L = 0$ to reduce those uncertainty contributions. Equation (6) implies that interferometers on either side of the beam line receive opposite phase shifts. Therefore, by moving the detector in the $\pm x$ direction, we observe linear changes in Φ as a function of Δx_{det} with slope $d\Phi/dx_{det}$ that is proportional to ΔL. Figure 4 shows data that demonstrate this effect. We set ΔL to 0 ± 30 μm by finding the ΔL for which $d\Phi/dx_{det} = 0$.

Since we recalibrate ΔL every day, the 30 μm uncertainty in ΔL represents a systematic error for one day's measurements and a statistical error for many days' measurements averaged together. That error will contribute toward the statistical
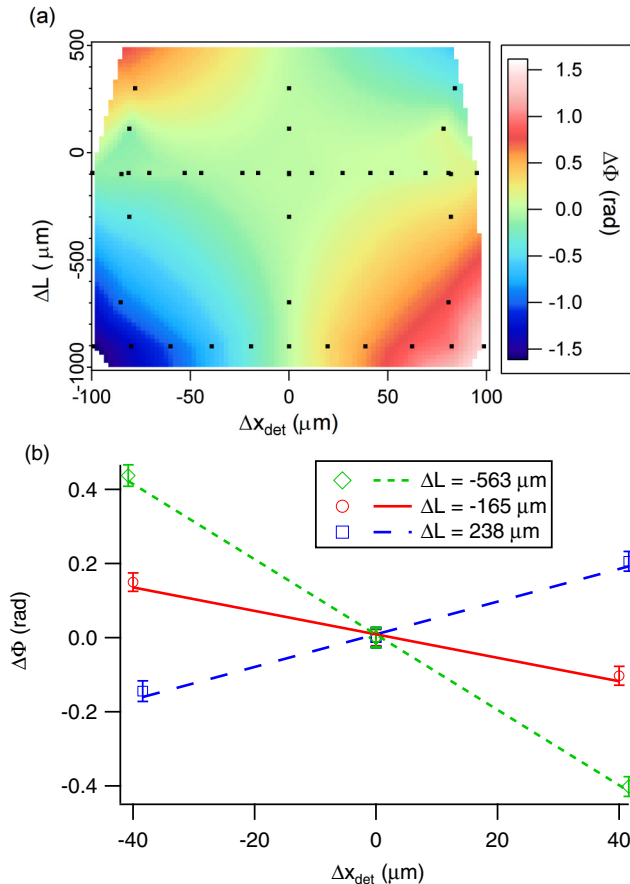
(a)

(b)

FIG. 4. (Color online) Two data plots showing how the phase Φ of the interference fringes changes linearly as a function of Δx_{det} and ΔL. In plot (a), the black dots represent coordinates at which data were acquired, and the colors represent contours inferred from the data. These figures show how Φ vs Δx_{det} is a line with slope proportional to ΔL.

uncertainty of α measurements. The same is true for $\Delta x_{det} = 0 \pm 30\ \mu m$, which also fluctuates from day to day as we set up the apparatus.

If the interferometer grating bars are significantly nonvertical, it becomes necessary to consider the phase shift induced by the component of gravitational acceleration in the plane of the interferometer. That phase shift is given by

$$\Delta\Phi_{accel} = \frac{\pi g \sin(\theta_g)(L_1 + L_2)^2}{2 d_g v^2}, \qquad (7)$$

where θ_g is the tilt of the grating bars with respect to vertical [31,32]. See [31] for an explanation of how we measured θ_g. Our interferometer's $|\theta_g|$ never exceeded 2.3 mrad. If we were to neglect this portion of the analysis, we would report v_0 incorrectly by up to 0.015% and v_r incorrectly by up to 0.25%.

The uncertainty budget for v_0 and v_r measurements is displayed in Fig. 5. The total statistical uncertainty in measured v_0 and v_r is roughly 10 times larger than the total systematic uncertainty after about 15 minutes of data acquisition with the phase choppers. Because v_0 and v_r drift over time, i.e., typically 3% over the course of several hours, we measure the velocity distribution twice every hour.
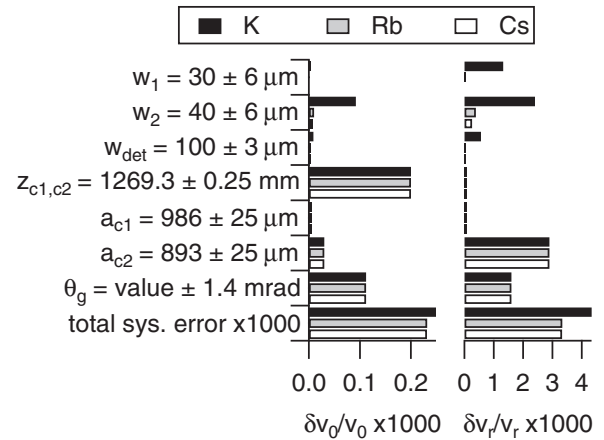

FIG. 5. Systematic uncertainty budget for measurements of v_0 and v_r for our Cs, Rb, and K beams. The total systematic error in v_0 and v_r in turn contributes toward the total systematic uncertainty in α measurements (shown in Fig. 7). A nominal value for θ_g is not listed because θ_g changed from -2.37 ± 1.39 to 1.73 ± 0.59 mrad toward the end of the experiment.

Gaseous alkali-metal atoms in an atomic beam nozzle have a probability of forming homonuclear dimers that depends on the gas pressure [33] and the diameter of the nozzle hole [34]. It is important for us to quantify the dimer mole fraction in our beam because the dimers' spatially averaged (tensor) polarizabilities are approximately 1.75 times the monomer polarizabilities [35]. In our nozzle, the vapor pressure of alkali-metal atoms is on the order of 1 torr at our typical running temperatures of 160 °C for Cs, 220 °C for Rb, and 350 °C for K. According to data acquired by Gordon *et al.* (1971) [33] and Bergmann *et al.* (1978) [34], our alkali-metal gas pressures of 1 torr should result in a dimer mole fraction well below 1%. Additionally, Holmgren *et al.* [11,36] demonstrated how to place an upper limit on the dimer mole fraction by analyzing resolved diffraction patterns through a single nanograting and looking for peaks associated with dimer diffraction. In this work, we used very similar nozzle temperatures in our experiment as Holmgren *et al.* did in 2010. For all of these reasons, we conclude that the dimer mole fraction in our beam must be less than 1%. Figure 7 shows how a 4% dimer mole fraction would lead to a significant (0.1%) error in measured polarizability.

C. Polarizability measurement

To measure the Cs, Rb, and K polarizability, we use two parallel, oppositely charged, 1/2-inch-diameter, stainless-steel pillars. The pillars are mounted to a single, rigid support structure so that a $3999.7 \pm 1.0\ \mu m$ gap exists between them. A motor moves the support structure in the $\pm x$ direction, and a length gauge monitors the structure's x position. The length gauge measures displacements of the structure with 30 nm accuracy. We begin a polarizability measurement with the assembly positioned such that the beam passes through the gap between the pillars near one of the edges. We take 25 sec of data with the electric field on and 25 sec with it off. We then move the pillars in nine 400 μm increments so
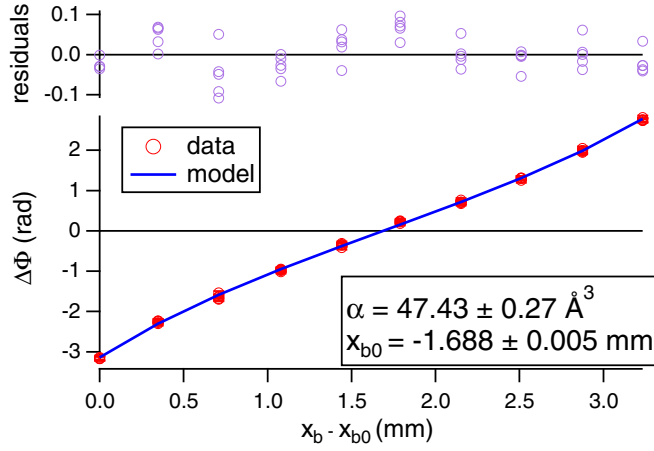
FIG. 6. (Color online) An example of a measurement of phase shift vs x position of the pillars for a Rb beam. The two fit parameters used to fit the model to these data are polarizability α_{Rb} and the pillars' position at which the phase shift is null x_{b0}.

that the beam approaches the other edge of the gap, taking 50 sec of data at each location. In doing so, we observe the phase shift $\Delta\Phi = \Phi_{pillars,on} - \Phi_{ref}$ applied by the pillars as a function of x_b (see an example in Fig. 6). We then repeat this sequence, moving the pillars in the opposite direction in order to minimize possible systematic errors associated with traveling in a certain direction. When the electric field is off, we observe the reference phase Φ_{ref} and reference contrast C_{ref} given by

$$C_{ref}e^{i\Phi_{ref}} = C_0 e^{i\Phi_0}\frac{1}{2}\sum_k \int_{v=0}^{\infty} P(v)e^{i\Delta\Phi_{sag}(v)}dv. \quad (8)$$

The Sagnac phase, $\Delta\Phi_{sag}$, is a phase shift caused by the Earth's rotation and is described in [11,37,38]. C_0 is the contrast that would be observed in the absence of $\Delta\Phi_{sag}(v)$, and Φ_0 is an arbitrary phase constant. When the field is on, we instead observe

$$C_{pillars,on}e^{i\Phi_{pillars,on}}$$
$$= C_0 e^{i\Phi_0}\frac{1}{2}\sum_k \int_{v=0}^{\infty} P(v)e^{i\Delta\Phi_{\bar{E},j}(v,x_b)+i\Delta\Phi_{sag}(v)}dv. \quad (9)$$

We fit a model to $\Delta\Phi$ vs x_b, as shown in Fig. 6. The fit parameters of that model are the polarizability and the pillars position x_{b0} for which the phase shift is zero (i.e., the location of the virtual ground plane).

In our earlier work, we used one pillar next to a grounded plate instead of two pillars forming a virtual ground plane [11]. We measured x_b by blocking the beam with the pillar. There were significant statistical errors of a few μm associated with this procedure, and a 1 μm error would lead to a 0.1% error in polarizability. Our new pillars assembly greatly reduces those statistical errors. Measuring $\Delta\Phi$ vs x_b on both sides of the ground plane makes our typical 5 μm uncertainties in x_{b0} add an insignificant amount of statistical uncertainty to the determined α.

The systematic uncertainty budget for our polarizability measurements is shown in Fig. 7. In the next few paragraphs,
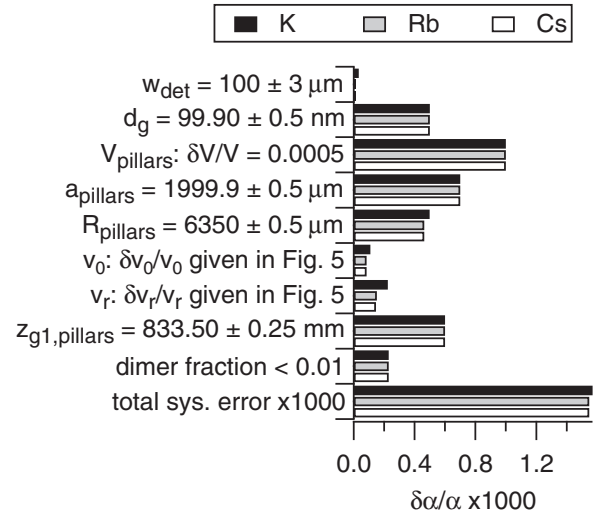

FIG. 7. Systematic uncertainty budget for polarizability measurements for our Cs, Rb, and K beams. The uncertainties in knowledge of v_0 and v_r are propagated forward from Fig. 5. Values of $V_{pillars}$ ranged from 5 to 7 kV, always with 0.05% uncertainty.

we discuss how we measured some of the quantities in the error budget.

We reduced the uncertainty in $V_{pillars}$ to 0.05% by independently calibrating our voltage supplies. To measure $V_{pillars}$, which ranged from 5 to 7 kV, we used a Fluke 80K-40 high-voltage probe. We measured the probe's voltage divider constant, which itself depended on input voltage, using two Fluke 287 digital multimeters.

We measured $z_{g1,pillars}$ to 1/4 mm accuracy. We placed rulers in the apparatus, after which three of us would read the rulers both live and from photographs. We repeated this process for many longitudinal positions of the rulers to further reduce statistical error in the measurement. Finally, we compared the rulers we used with other rulers to verify that the ones we used were printed without significant systematic error. The value of $z_{g1,pillars}$ we use in this analysis is the average of all those measurements.

We measured the width of the gap between the pillars, $2a_{pillars}$, to 1 μm accuracy by repeatedly scanning the pillars assembly across the beam and recording the positions at which each pillar blocked half of the atom beam. To verify that $a_{pillars}$ did not change over time, we repeated this procedure many times throughout the months during which we acquired our data.

Our θ_g was always close enough to zero such that we did not need to consider $\Delta\Phi_{accel}$ in our polarizability data analysis. We would only need to consider $\Delta\Phi_{accel}$ if $|\theta_g|$ exceeded 23 mrad. We also find that uncertainties in w_1 and w_2 each do not correspond to more than 0.004% uncertainty in α.

D. Determining the velocity distribution during polarizability measurements

A typical sequence of measurements is shown in Table II. We measure the velocity distribution twice between every four scans of the pillars across the beam, and calibrate the phase choppers between each pair of velocity measurements.

TABLE II. A typical sequence of measurements during a day of data acquisition. The $+x$ direction is arbitrarily chosen—the important aspect is that we spend an equal amount of time scanning the pillars in each direction so as to minimize possible systematic errors. This sequence of eight measurements is repeated once per hour for anywhere between 8 and 36 hours. We end the data acquisition by repeating the first four measurements.

Type of data acquired	Duration
contrast vs chopping freq.	7m 5s
chopper c1 phase	3m 45s
chopper c2 phase	3m 45s
contrast vs chopping freq.	7m 5s
$\Delta\Phi$ vs pillars position ($+x$ direction)	8m 45s
$\Delta\Phi$ vs pillars position ($-x$ direction)	8m 45s
$\Delta\Phi$ vs pillars position ($+x$ direction)	8m 45s
$\Delta\Phi$ vs pillars position ($-x$ direction)	8m 45s

We linearly interpolate between v_0 and v_r measurements before and after each pillars scan to estimate those quantities at the time of that scan. Using cubic spline interpolation and Gaussian process regression to interpolate between v_0 and v_r measurements changes our reported polarizabilities by no more than 0.001%, which is small compared to our other uncertainties.

III. RESULTS AND DISCUSSION

Table III shows our measurement results for the K, Rb, and Cs atomic polarizabilities, α_K, α_{Rb}, and α_{Cs}. The tabulated statistical uncertainties are the standard error of the mean for each result. To get this statistical precision, we acquired over 90 hours of data, including 150 data sets similar to Fig. 6 and 60 data sets similar to Fig. 3. The total systematic uncertainty for each measurement is also stated in Table III, and a breakdown of the systematic uncertainty budget is summarized in Fig. 7. While the statistical uncertainties are typically 0.05% for our measurements of polarizabilities, the systematic uncertainties are three to four times larger and cause a total uncertainty of typically 0.16% for each measurement.

We report the ratios of polarizabilities α_{Cs}/α_K, α_{Cs}/α_{Rb}, and α_{Rb}/α_K in Table IV. These ratios have uncertainties smaller than 0.08% because we used the same apparatus for each direct measurement. For many of the sources of systematic uncertainty summarized in Fig. 7, an error in one of those quantities would scale each direct polarizability measurement by the same amount. These correlated uncertainties, such as electrode geometry or grating pitch, do not contribute

TABLE IV. Measured ratios of Cs, Rb, and K static, ground-state polarizabilities. The systematic uncertainties in each ratio, which arise from the fact that the systematic errors in different measurements are not perfectly correlated, are negligible compared to the statistical uncertainties.

Ratio	Value(stat.)	Sys. errors
α_{Cs}/α_K	1.3834(9)	3×10^{-5}
α_{Cs}/α_{Rb}	1.2532(10)	7×10^{-7}
α_{Rb}/α_K	1.1040(9)	2×10^{-5}

significantly to systematic errors in our measured polarizability ratios. However, uncertainties in w_1, w_2, w_{det}, and ΔL affect our α_K, α_{Rb}, and α_{Cs} measurements differently and therefore contribute a small amount to the final systematic uncertainties in the ratios. Even so, the ratios' systematic errors are much smaller than the statistical uncertainties. We discuss the value of high-precision ratios for testing atomic theories in Sec. III A, and we discuss the possibility of using such ratios to improve individual measurements of polarizability in Sec. IV.

A. Comparisons with other experimental and theoretical polarizabilities

Figure 8 and Table VIII compare our polarizability measurements with *ab initio* calculations, semiempirical calculations, and experimental measurements subsequent to and including Molof *et al.*'s and Hall *et al.*'s 1974 measurements [4,7]. First, we will discuss the comparison to previous direct measurements. Our K and Rb polarizability measurements have three times smaller uncertainty than our group's previously published direct measurements of α_K and α_{Rb} [11], and ten times smaller uncertainty than the only other direct measurements of α_K and α_{Rb}, which were made using the E-H gradient balance technique [7] and the E gradient deflection technique [4]. We emphasize that our measurements are independent of the results in [11] because although we used the same atom interferometer machine, we used a different material nanograting g1, different electrodes with different geometry, a different atom beam velocity measurement technique, a different atom beam source nozzle, and a detector with a different width. Hence, the fact that our latest and more precise measurements are consistent with the measurements in [4,7,11] should be regarded as an independent validation of each of these previous results.

TABLE III. Direct measurements of Cs, Rb, and K static, ground-state polarizabilities.

Atom	α(stat.)(sys.) (Å^3)
Cs	59.39(3)(9)
Rb	47.39(3)(8)
K	42.93(2)(7)

TABLE V. We use the following residual polarizabilities α_r and matrix element ratios $R = D_{3/2}^2/D_{1/2}^2$. The sources for each quantity are cited next to the values in the table.

Atom	α_r (Å^3)	R
Cs	2.481(16) [17]	1.9809(9) [73]
Rb	1.562(89) [79]	1.996(4) [65]
K	0.925(45) [79]	2.000(4) [80]

TABLE VI. Matrix elements, lifetimes, oscillator strengths, line strengths, and van der Waals C_6 coefficients calculated from our polarizability measurements. We used R values from Table V. The matrix elements, line strengths, and C_6 coefficient are expressed in atomic units, while the lifetimes are expressed in SI units. δ_α, δ_R, and δ_{α_r} represent the uncertainties in the values due to uncertainty in α, R, and α_r, respectively. $\delta_{\rm tot}$ is the total uncertainty in the value. (-) represents a nonzero uncertainty of less than 0.5.

Quantity	Atom	Value	δ_α	δ_R	δ_{α_r}	$\delta_{\rm tot}$
$D_{1/2}$	Cs	4.508	(4)	(1)	(1)	(4)
	Rb	4.239	(4)	(3)	(4)	(6)
	K	4.101	(3)	(3)	(2)	(5)
$D_{3/2}$	Cs	6.345	(5)	(-)	(1)	(5)
	Rb	5.989	(5)	(2)	(6)	(8)
	K	5.800	(5)	(2)	(3)	(6)
$\tau_{1/2}$ (ns)	Cs	34.77	(5)	(1)	(1)	(6)
	Rb	27.60	(5)	(4)	(5)	(8)
	K	26.81	(4)	(4)	(3)	(6)
$\tau_{3/2}$ (ns)	Cs	30.37	(5)	(-)	(1)	(5)
	Rb	26.14	(5)	(2)	(5)	(7)
	K	26.45	(4)	(2)	(3)	(6)
$f_{1/2}$	Cs	0.3450	(5)	(1)	(1)	(6)
	Rb	0.3433	(6)	(5)	(7)	(10)
	K	0.3317	(6)	(4)	(4)	(8)
$f_{3/2}$	Cs	0.7174	(11)	(1)	(2)	(12)
	Rb	0.6982	(12)	(5)	(14)	(19)
	K	0.6665	(11)	(4)	(7)	(14)
$S_{1/2}$	Cs	20.32	(3)	(1)	(1)	(3)
	Rb	17.97	(3)	(3)	(3)	(5)
	K	16.82	(3)	(2)	(2)	(4)
$S_{3/2}$	Cs	40.26	(6)	(1)	(1)	(6)
	Rb	35.87	(6)	(3)	(7)	(10)
	K	33.64	(6)	(2)	(4)	(7)
C_6	Cs	6879	(20)	(-)	(7)	(21)
	Rb	4719	(15)	(-)	(26)	(30)
	K	3884	(13)	(-)	(14)	(19)

There is one other direct measurement of $\alpha_{\rm Cs}$ with uncertainty similar to (and slightly smaller than) ours. Our direct $\alpha_{\rm Cs}$ measurement is 11 times more precise than the result reported using the E-H balance technique [7], but 1.1 times less precise than Amini and Gould's 2003 measurement [8] that was made using an atomic fountain apparatus. To our knowledge, Amini

TABLE VII. Excited-state polarizabilities $\alpha_{np_{1/2}}$, where $n = 6$ for Cs, $n = 5$ for Rb, and $n = 4$ for K. The values were calculated using our measurements and $\alpha_{np_{1/2}} - \alpha_{ns_{1/2}}$ measurements [86,87].

Atom	$\alpha_{np_{1/2}}$ ($\mathring{\rm A}^3$)
Cs	196.81(9)
Rb	120.33(8)
K	89.92(7)

and Gould's work is the only polarizability measurement to date that has been accomplished using an atomic fountain, and it produced a remarkable improvement in precision by a factor of 15 as compared to the only previous direct measurements of $\alpha_{\rm Cs}$ [4,7]. Furthermore, $\alpha_{\rm Cs}$ measurements can test some of the atomic structure theory that is used to interpret atomic parity-nonconservation experiments as a way of constraining physics beyond the standard model [15–18]. Thus, it is particularly important to validate this $\alpha_{\rm Cs}$ result in [8]. We find that our $\alpha_{\rm Cs}$ measurement is consistent with Amini and Gould's. Our result $\alpha_{\rm Cs} = 59.39(9)\ \mathring{\rm A}^3$ deviates from their result of $\alpha_{\rm Cs} = 59.42(8)\ \mathring{\rm A}^3$ by $0.03\ \mathring{\rm A}^3$, which is insignificant. Comparing our atom interferometer result with their fountain result serves as a cross check for both methods. Both measurements also agree with $\alpha_{\rm Cs}$ values inferred from the atomic structure calculations by Derevianko and Porsev (2002) [17] and Derevianko *et al.* (1999) [50] for PNC analysis.

Most theoretical predictions for $\alpha_{\rm K}$, $\alpha_{\rm Rb}$, and $\alpha_{\rm Cs}$ deviate from each other and from our measurements significantly. Out of 28 sets of theoretical predictions shown in Fig. 8, only ten sets of predictions [17,50,55–62] are consistent with our results within 3σ (where σ is the standard deviation of our measurement). Furthermore, the semiempirical $\alpha_{\rm K}$, $\alpha_{\rm Rb}$, and $\alpha_{\rm Cs}$ values calculated in 1999 by Derevianko *et al.* [50] are the only predictions that match all three of our own $\alpha_{\rm K}$, $\alpha_{\rm Rb}$, and $\alpha_{\rm Cs}$ measurements to within 3σ. These predictions [50] were made using measured lifetimes and energies, and Derevianko and Porsev's later $\alpha_{\rm Cs}$ prediction [17] was made using a measured van der Waals C_6 coefficient. This is an important point because there are now additional data on lifetimes, van der Waals C_6 measurements, and line strength ratios that can inform new semiempirical predictions for polarizabilities that we discuss in Sec. III B and Fig. 9.

Figure 8(b) compares our measurements of atomic polarizability ratios to other theoretical, semiempirical, and experimental reports for these ratios. The values we measured for $\alpha_{\rm Cs}/\alpha_{\rm K}$, $\alpha_{\rm Cs}/\alpha_{\rm Rb}$, and $\alpha_{\rm Rb}/\alpha_{\rm K}$ are consistent with all of the previous experimental measurements of these ratios, given the larger uncertainties associated with previous measurements. Comparing theoretical predictions to our measured polarizability ratios serves as a different way to test the theoretical predictions. Since the fractional uncertainties on our measured ratios are smaller than those of our absolute measurements, our ratios serve as a more precise test for theoretical works that predict α values for multiple alkali-metal atoms.

B. Comparisons with polarizabilities derived from other quantities

Static polarizabilities can be related to electric-dipole transition-matrix elements, state lifetimes, oscillator strengths, and van der Waals coefficients. We will describe those relations and compare our α measurements to α values derived from recent calculations and high-precision measurements of those quantities. Those comparisons are shown in Fig. 9 and Table VIII.
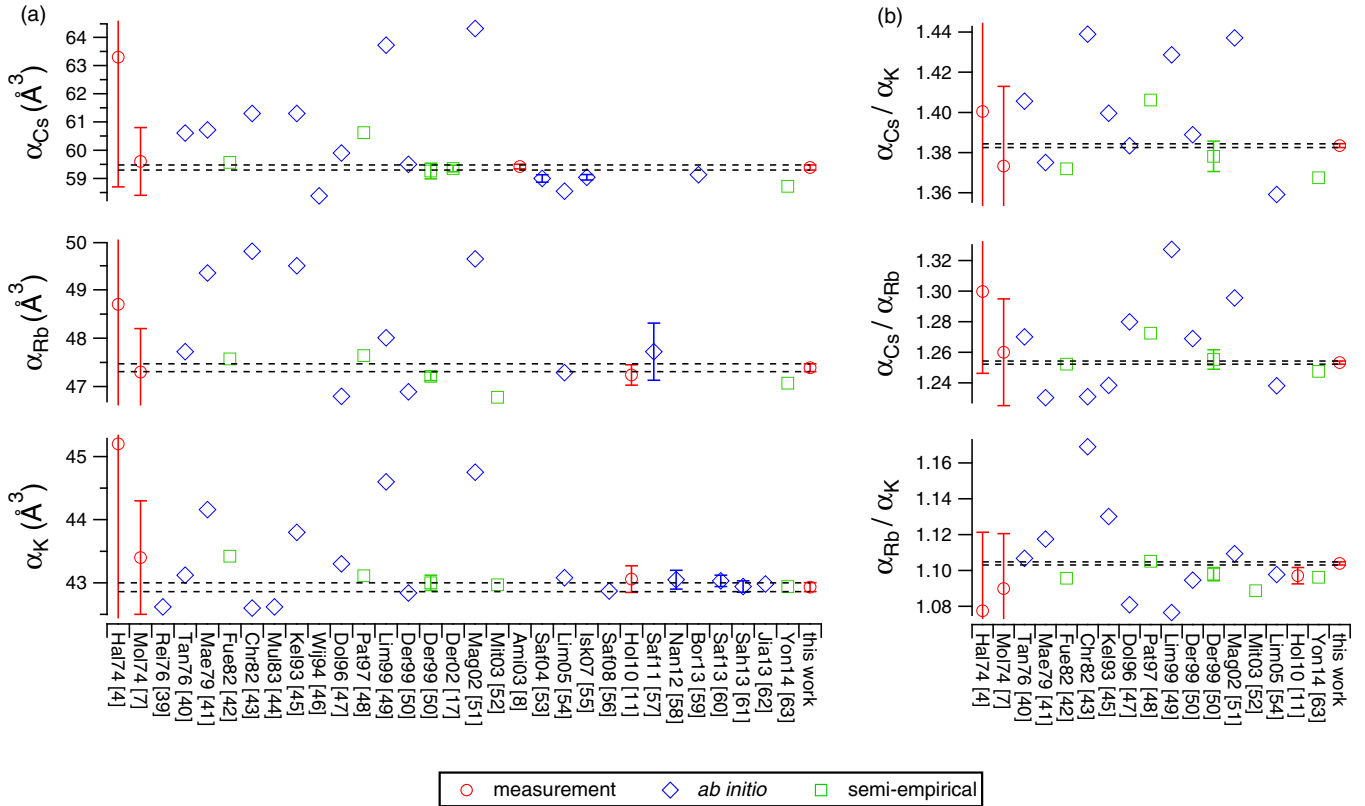
FIG. 8. (Color online) Our (a) direct measurements and (b) measured ratios compared with other measurements, *ab initio* calculations, and semiempirical calculations [4,7,8,11,17,39–60,60–63]. The references are represented on the *x* axis by the first three letters of the first author's last name, followed by the year of publication. For the semiempirical calculations: Reference Fue82 used semiempirical pseudopotentials [42], Pat97 used experimentally determined energy levels [48], Der99 used experimentally determined electric-dipole transition matrix elements [50], and Mit03 and Yon14 used semiempirical core polarization potentials [52,63]. Values in this plot from 1999 and later are also reported in Table VIII at the end of this paper.

The polarizability (in volume units) of an atom in state i can be written in terms of Einstein A coefficients A_{ij} as

$$\alpha_i = \frac{c^3}{2} \sum_{j \neq i} \frac{A_{ij}}{\omega_{ij}^4} \frac{g_j}{g_i} + \alpha_r, \qquad (10)$$

where ω_{ik} is the transition frequency between states i and k, and $g_n = 2J_n + 1$ is the degeneracy factor for state n. In our case, state i is the ground state. The residual polarizability α_r includes terms not explicitly included in the sum, the polarizability of the core electrons, and a correction accounting for correlations between core and valence electrons as described in several references [17,50,79]. We will explicitly sum over the principal transitions from $ns_{1/2}$ to $np_{1/2}$ and $np_{3/2}$, where $n = 6$ for Cs, $n = 5$ for Rb, and $n = 4$ for K, and we will include the other transitions in α_r. We abbreviate the lifetimes associated with the principal transitions to $\tau_{1/2}$ and $\tau_{3/2}$. In our calculations, we use the transition wavelengths ω_{ik} from Refs. [81–84] and the α_r values indicated in Table V. Figure 9 shows polarizabilities calculated using measurements of $\tau_{1/2}$ and $\tau_{3/2}$ [64–66,68–70,72]. Figure 9 also shows α_{Cs} calculated from values of $\tau_{1/2,Rb}$ and $\tau_{3/2,Rb}$ inferred in 2002 by Gutterres *et al.* from photoassociation data taken in 2000 by Gabbanini *et al.* [74,75].

We can use Patterson *et al.*'s 2015 measurement of $\tau_{3/2,Cs}$ [85] along with a measurement of the ratio of principal transition-matrix elements to report α_{Cs}. Rafac and Tanner measured the ratio of Cs electric-dipole transition-matrix elements [73],

$$R_{Cs} = \frac{|\langle 6s_{1/2} \| \hat{D} \| 6p_{3/2} \rangle|^2}{|\langle 6s_{1/2} \| \hat{D} \| 6p_{1/2} \rangle|^2}, \qquad (11)$$

which is related to the ratio of lifetimes,

$$\frac{\tau_{1/2}}{\tau_{3/2}} = \frac{R_{Cs}}{2} \left(\frac{\omega_{3/2}}{\omega_{1/2}} \right)^3. \qquad (12)$$

We can also report a polarizability using R_{Cs} [73] in conjunction with Porsev *et al.*'s 2010 calculation of $D_{1/2,Cs}^2 = 20.334$ (in atomic units) [76]. We can write α_i in terms of the electric-dipole transition-matrix elements as

$$\alpha_i = \frac{e^2}{12\pi \epsilon_0 a_0^4} \sum_{j \neq i} \frac{|\langle i \| \hat{D} \| j \rangle|^2}{\hbar \omega_{ij}} + \alpha_r, \qquad (13)$$

where a_0 is the Bohr radius. As before, we only explicitly consider the $ns_{1/2} - np_{1/2}$ and $ns_{1/2} - np_{3/2}$ matrix elements, where $ns_{1/2}$ is the ground state. We abbreviate the matrix

TABLE VIII. Comparisons of directly measured, semiempirical, and *ab initio* polarizabilities from 1999 and later. These values are also plotted in Figs. 8 and 9. Lines with α_r in the Method column were calculated using residual polarizabilities α_r in Table V [17,79]. Ratios of polarizabilities $\alpha_{Rb}/\alpha_K = 1.097(5)$ from [11] and $\alpha_{Cs}/\alpha_{Rb} = 1.2532(10)$, $\alpha_{Cs}/\alpha_K = 1.3834(9)$, $\alpha_{Rb}/\alpha_K = 1.1040(9)$ from this work have been reported with smaller fractional uncertainties than the direct measurements listed in this table. For the *ab initio* method acronyms: CCSD indicates the coupled-cluster approach with single and double excitations of the wave functions. The prefix R stands for "relativistic" and the prefix L stands for "linearized." The suffix T indicates that the authors used perturbative triple excitations of the wave functions. See [1] for explanations of these various theoretical methods.

Reference(s)	Method	α_{Cs} (Å^3)	α_{Rb} (Å^3);	α_K (Å^3);
Raf99 [17,69]	$\tau_{1/2}, \tau_{3/2}$ meas. $+ \alpha_r$	58.97(10)		
Der99 [50]	*ab initio*, RLCCSD	59.50	46.89	42.84
Der99 [50]	semiempirical	59.26(28)	47.21(9)	43.00(12)
Leo00 [17,73,77]	C_6 meas. $+ R_{Cs}$ meas. $+$ thry $+ \alpha_r$	59.49(25)		
Gut02 [74,75,79]	$\tau_{1/2}, \tau_{3/2}$ from PA data $+ \alpha_r$		47.18(14)	
Der02 [17]	semiempirical	59.35(12)		
Mag02 [51]	*ab initio*	64.31	49.64	44.75
Ami03 [8]	direct α_{Cs} meas.	59.42(8)		
Mit03 [52]	semiempirical		46.78	42.97
Chi04 [17,73,78]	C_6 meas. $+ R_{Cs}$ meas. $+$ thry $+ \alpha_r$	59.35(22)		
Saf04 [53]	*ab initio*	59.00(13)		
Lim05 [54]	*ab initio*, RCCSDT	58.55	47.29	43.08
Fal06 [70,79]	$\tau_{1/2}, \tau_{3/2}$ meas. $+ \alpha_r$			43.02(6)
Bou07 [17,72]	$\tau_{1/2}, \tau_{3/2}$ meas. $+ \alpha_r$	59.31(40)		
Isk07 [55]	*ab initio*, RLCCSDT	59.04(10)		
Saf08 [56]	*ab initio*, RLCCSDT			42.87
Hol10 [11]	direct α_{Rb} and α_K meas.		47.24(44)	43.06(36)
Hol10 [9,11]	ratio calibrated with α_{Na}		47.24(21)	43.06(21)
Por10 [17,73,76]	*ab initio* $D_{1/2}^2 + R_{Cs}$ meas. $+ \alpha_r$	59.42(3)		
Saf11 [57]	*ab initio*, RCCSD		47.72(59)	
Nan12 [58]	*ab initio*, RCCSDT			43.05(15)
Bor13 [59]	*ab initio*, RCCSDT	59.13		
Saf13 [60]	*ab initio*, RLCCSDT			43.03(9)
Sah13 [61]	*ab initio*, RCCSDT			42.94(9)
Jai13 [62]	semiempirical			42.98
Yon14 [63]	semiempirical	58.72	47.07	42.94
Pat15 [17,73,85]	$\tau_{3/2}$ meas. $+ R_{Cs}$ meas. $+ \alpha_r$	59.21(7)		
This work	direct meas.	59.39(9)	47.39(8)	42.93(7)

elements associated with the principal transitions to $D_{1/2}$ and $D_{3/2}$.

In 2002, Derevianko and Porsev demonstrated a method for obtaining values of $D_{1/2,Cs}^2$ and $D_{3/2,Cs}^2$ from Cs van der Waals C_6 coefficients [17] and R_{Cs} [73]. Figure 9 includes α values derived using experimental Cs C_6 measurements in conjunction with that method [77,78].

C. Other atomic properties derived from our polarizability measurements

Finally, we use our polarizability measurements to report matrix elements, lifetimes, oscillator strengths, line strengths, and van der Waals C_6 coefficients. These results are shown in Table VI. In these calculations, we use residual polarizabilities α_r and matrix element ratios R from Table V. To report matrix elements and lifetimes, we use Eqs. (13) and (10). α_i is given in terms of oscillator strengths f_{ij} as

$$\alpha_i = \frac{e^2}{4\pi\epsilon_0 m} \sum_{j \neq i} \frac{f_{ij}}{w_{ij}^2} + \alpha_r, \quad (14)$$

where m is the electron mass. α_i is also given in terms of line strengths S_{ji} as

$$\alpha_i = \frac{1}{6\pi\epsilon_0 \hbar} \sum_{j \neq i} \frac{S_{ji}}{g_i \omega_{ij}} + \alpha_r. \quad (15)$$

C_6 can be expressed in terms of dynamic polarizability as

$$C_6 = \frac{3}{\pi} \int_0^\infty \alpha(i\omega)^2 d\omega. \quad (16)$$

Derevianko *et al.*'s 2010 work tabulates values of $\alpha(i\omega)$ for Cs, Rb, and K atoms, among others [88]. To derive C_6 values from our $\alpha(0)$ measurements, we modify Derevianko *et al.*'s values of $\alpha(i\omega)$ to get

$$\alpha_{new}(i\omega) = \tilde{\alpha}(i\omega) + [\alpha_{thiswork}(0) - \tilde{\alpha}(0)]\frac{\alpha_p(i\omega)}{\alpha_p(0)}, \quad (17)$$

where $\tilde{\alpha}(i\omega)$ and $\tilde{\alpha}(0)$ refer to values tabulated by Derevianko *et al.* In the above equation (17), $\alpha_p(i\omega)$ is the contribution to $\alpha(i\omega)$ by the principle transitions. The ratio $\alpha_p(i\omega)/\alpha_p(0)$ is
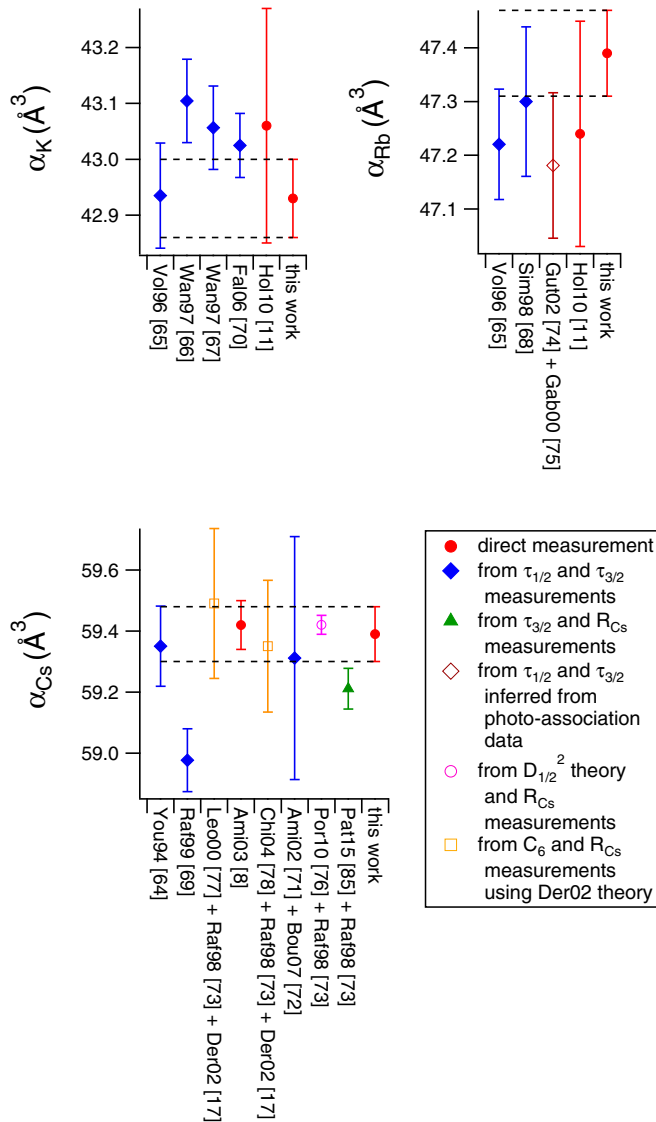
FIG. 9. (Color online) Comparisons of our laboratory's polarizability measurements (this work as well as [11]) and Amini and Gould's α_{Cs} measurement [8] to polarizabilities derived from measured lifetimes and lifetime ratios [64–73], lifetimes inferred from photoassociation data [74,75], theoretical D^2 values [76], and van der Waals C_6 measurements [17,77,78]. Values in this plot from 1999 and later are also reported in Table VIII at the end of this paper.

given by

$$\frac{\alpha_p(i\omega)}{\alpha_p(0)} = \frac{\frac{1}{\omega_{1/2}^2 + \omega^2} + \frac{R\frac{\omega_{1/2}}{\omega_{3/2}}}{\omega_{3/2}^2 + \omega^2}}{\frac{1}{\omega_{1/2}^2} + R\frac{\omega_{1/2}}{\omega_{3/2}^3}}. \tag{18}$$

Predictions of the parity-nonconserving amplitude, E_{PNC}, in Cs depend heavily on $D_{1/2}$. We note that our Cs $D_{1/2}$ value is consistent with the theoretical Cs $D_{1/2}$ calculated by Porsev *et al.* in 2010 for the purpose of interpreting PNC data as a test of the standard model [76].

Finally, we use our measurements together with recent measurements of Cs, Rb, and K $\alpha_{np_{1/2}} - \alpha_{ns_{1/2}}$ [86,87] to report excited-state polarizabilities $\alpha_{np_{1/2}}$ with better than 0.08% uncertainty. These results are shown in Table VII and serve as benchmark tests for calculations of dipole transition-matrix elements for $p - d$ transitions.

IV. OUTLOOK

We are currently exploring ways to measure the polarizability of Li and metastable He, the polarizabilities of which can be accurately calculated. By measuring α_{Cs}/α_{He*} or α_{Cs}/α_{Li}, we could report α_{Cs} with precision comparable to that of the ratios reported here for the benefit of PNC research. Such a measurement would also act as a calibration of the measurements presented in this work because it would be independent of systematic errors that may affect our direct measurements.

We are also exploring electron-impact ionization schemes for atom detection, which would allow us to detect most atoms and molecules. Our Langmuir-Taylor detector only allows us to detect alkali metals and some alkaline-Earth metals [21]. Installing an electron-impact ionization detector would allow us to broaden the scope of atom interferometry as a precision measurement tool.

[1] J. Mitroy, M. S. Safronova, and C. W. Clark, Theory and applications of atomic and ionic polarizabilities, J. Phys. B **43**, 202001 (2010).

[2] H. Scheffers and J. Stark, Einfluss des elektrischen Feldes auf Alkaliatome im Atomstrahlversuch, Phys. Z. **35**, 625 (1934).

[3] G. E. Chamberlain and J. C. Zorn, Alkali polarizabilities by the atomic beam electrostatic deflection method, Phys. Rev. **129**, 677 (1963).

[4] W. D. Hall and J. C. Zorn, Measurement of alkali-metal polarizabilities by deflection of a velocity-selected atomic beam, Phys. Rev. A **10**, 1141 (1974).

[5] L. Ma, J. Indergaard, B. Zhang, I. Larkin, R. Moro, and W. A. de Heer, Measured atomic ground-state polarizabilities of 35 metallic elements, Phys. Rev. A **91**, 010501 (2015).

[6] A. Salop, E. Pollack, and B. Bederson, Measurements of the electric polarizabilities of the alkalis using the E-H gradient balance method, Phys. Rev. **124**, 1431 (1961).

[7] R. W. Molof, H. L. Schwartz, T. M. Miller, and B. Bederson, Measurements of electric dipole polarizabilities of the alkali-metal atoms and the metastable noble-gas atoms, Phys. Rev. A **10**, 1131 (1974).

[8] J. M. Amini and H. Gould, High Precision Measurement of the Static Dipole Polarizability of Cesium, Phys. Rev. Lett. **91**, 153001 (2003).

[9] C. R. Ekstrom, J. Schmiedmayer, M. S. Chapman, T. D. Hammond, and D. E. Pritchard, Measurement of the electric polarizability of sodium with an atom interferometer, Phys. Rev. A **51**, 3883 (1995).

[10] A. Miffre, M. Jacquey, M. Büchner, G. Trénec, and J. Vigué, Atom interferometry measurement of the electric polarizability of lithium, Eur. Phys. J. D **38**, 353 (2006).

[11] W. F. Holmgren, M. C. Revelle, V. P. A. Lonij, and A. D. Cronin, Absolute and ratio measurements of the polarizability of Na, K, and Rb with an atom interferometer, Phys. Rev. A **81**, 053607 (2010).

[12] M. Berninger, A. Stefanov, S. Deachapunya, and M. Arndt, Polarizability measurements of a molecule via a near-field matter-wave interferometer, Phys. Rev. A **76**, 013607 (2007).

[13] *Atom Interferometry*, edited by P. Berman (Academic, San Diego, 1997).

[14] A. D. Cronin, J. Schmiedmayer, and D. E. Pritchard, Optics and interferometry with atoms and molecules, Rev. Mod. Phys. **81**, 1051 (2009).

[15] S. A. Blundell, J. Sapirstein, and W. R. Johnson, High-accuracy calculation of parity nonconservation in cesium and implications for particle physics, Phys. Rev. D **45**, 1602 (1992).

[16] D. Cho, C. S. Wood, S. C. Bennett, J. L. Roberts, and C. E. Wieman, Precision measurement of the ratio of scalar to tensor transition polarizabilities for the cesium 6S-7S transition, Phys. Rev. A **55**, 1007 (1997).

[17] A. Derevianko and S. G. Porsev, High-precision determination of transition amplitudes of principal transitions in Cs from van der Waals coefficient C_6, Phys. Rev. A **65**, 053403 (2002).

[18] S. G. Porsev, K. Beloy, and A. Derevianko, Precision Determination of Electroweak Coupling from Atomic Parity Violation and Implications for Particle Physics, Phys. Rev. Lett. **102**, 181601 (2009).

[19] M.-A. Bouchiat and C. Bouchiat, Parity violation in atoms, Rep. Prog. Phys. **60**, 1351 (1997).

[20] V. A. Dzuba, J. C. Berengut, V. V. Flambaum, and B. Roberts, Revisiting Parity Nonconservation in Cesium, Phys. Rev. Lett. **109**, 203003 (2012).

[21] R. Delhuille, A. Miffre, E. Lavallette, M. Büchner, C. Rizzo, G. Trénec, J. Vigué, H. J. Loesch, and J. P. Gauyacq, Optimization of a Langmuir-Taylor detector for lithium, Rev. Sci. Instrum. **73**, 2249 (2002).

[22] T. D. Roberts, Measuring atomic properties with an atom interferometer, Ph.D. thesis, Massachusetts Institute of Technology, 2002.

[23] T. D. Roberts, A. D. Cronin, M. V. Tiberg, and D. E. Pritchard, Dispersion Compensation for Atom Interferometry, Phys. Rev. Lett. **92**, 060405 (2004).

[24] W. F. Holmgren, I. Hromada, C. E. Klauss, and A. D. Cronin, Atom beam velocity measurements using phase choppers, New J. Phys. **13**, 115007 (2011).

[25] I. Hromada, R. Trubko, W. F. Holmgren, M. D. Gregoire, and A. D. Cronin, de Broglie wave-front curvature induced by electric-field gradients and its effect on precision measurements with an atom interferometer, Phys. Rev. A **89**, 033612 (2014).

[26] *Atomic and Molecular Beam Methods*, edited by G. Scoles, D. Bassi, U. Buck, and D. Lainé (Oxford University Press, New York, 1988).

[27] C. R. Ekstrom, Experiments with a separated beam atom interferometer, Ph.D. thesis, Massachusetts Institute of Technology, 1993.

[28] T. A. Savas, S. N. Shah, M. L. Schattenburg, J. M. Carter, and H. I. Smith, Achromatic interferometric lithography for 100-nm-period gratings and grids, J. Vac. Sci. Technol. B **13**, 2732 (1995).

[29] T. A. Savas, Achromatic interference lithography, Ph.D. thesis, Massachusetts Institute of Technology, 2003.

[30] D. A. Kokorowski, Measuring decoherence and the matter-wave index of refraction with an improved atom interferometer, Ph.D. thesis, Massachusetts Institute of Technology, 2001.

[31] J. Greenberg (unpublished).

[32] R. Trubko, J. Greenberg, M. T. St. Germaine, M. D. Gregoire, W. F. Holmgren, I. Hromada, and A. D. Cronin, Atom Interferometer Gyroscope with Spin-Dependent Phase Shifts Induced by Light Near a Tune-Out Wavelength, Phys. Rev. Lett. **114**, 140404 (2015).

[33] R. J. Gordon, Y. T. Lee, and D. R. Herschbach, Supersonic molecular beams of alkali dimers, J. Chem. Phys. **54**, 2393 (1971).

[34] K. Bergmann, U. Hefter, and P. Hering, Molecular beam diagnostics with internal state selection: velocity distribution and dimer formation in a supersonic Na/Na_2 beam, Chem. Phys. **32**, 329 (1978).

[35] V. Tarnovsky, M. Bunimovicz, L. Vuskovic, B. Stumpf, and B. Bederson, Measurements of the dc electric dipole polarizabilities of the alkali dimer molecules, homonuclear and heteronuclear, J. Chem. Phys. **98**, 3894 (1993).

[36] W. F. Holmgren, Polarizability and magic-zero wavelength measurements of alkali atoms, Ph.D. thesis, University of Arizona, 2013.

[37] A. Lenef, T. D. Hammond, E. T. Smith, M. S. Chapman, R. A. Rubenstein, and D. E. Pritchard, Rotation Sensing with an Atom Interferometer, Phys. Rev. Lett. **78**, 760 (1997).

[38] M. Jacquey, A. Miffre, G. Trénec, M. Büchner, J. Vigué, and A. Cronin, Dispersion compensation in atom interferometry by a Sagnac phase, Phys. Rev. A **78**, 013638 (2008).

[39] E. A. Reinsch and W. Meyer, Finite perturbation calculation for the static dipole polarizabilities of the atoms Na through Ca, Phys. Rev. A **14**, 915 (1976).

[40] K. T. Tang, Upper and lower bounds of two- and three-body dipole, quadrupole, and octupole van der Waals coefficients for hydrogen, noble gas, and alkali atom interactions, J. Chem. Phys. **64**, 3063 (1976).

[41] F. Maeder and W. Kutzelnigg, Natural states of interacting systems and their use for the calculation of intermolecular forces, Chem. Phys. **35**, 397 (1979).

[42] P. Fuentealba, On the reliability of semiempirical pseudopotentials: dipole polarisability of the alkali atoms, J. Phys. B **15**, L555 (1982).

[43] P. A. Christiansen and K. S. Pitzer, Reliable static electric dipole polarizabilities for heavy elements, Chem. Phys. Lett. **85**, 434 (1982).

[44] W. Müller, J. Flesch, and W. Meyer, Treatment of intershell correlation effects in *ab initio* calculations by use of core polarization potentials. Method and application to alkali and alkaline earth atoms, J. Chem. Phys. **80**, 3297 (1984).

[45] V. Kello, A. J. Sadlej, and K. Faegri, Electron-correlation and relativistic contributions to atomic dipole polarizabilities: Alkali-metal atoms, Phys. Rev. A **47**, 1715 (1993).

[46] W. A. van Wijngaarden and J. Li, Polarizabilities of Cesium S, P, D, and F States, J. Quantum Spectrosc. Radiat. Transf. **52**, 555 (1994).

[47] M. Dolg, Fully relativistic pseudopotentials for alkaline atoms: Dirac–Hartree–Fock and configuration interaction calculations of alkaline monohydrides, Theor. Chim. Acta **93**, 141 (1996).

[48] S. H. Patil and K. T. Tang, Multipolar polarizabilities and two- and three-body dispersion coefficients for alkali isoelectronic sequences, J. Chem. Phys. **106**, 2298 (1997).

[49] I. S. Lim, M. Pernpointner, M. Seth, J. K. Laerdahl, P. Schwerdt-feger, P. Neogrady, and M. Urban, Relativistic coupled-cluster static dipole polarizabilities of the alkali metals from Li to element 119, Phys. Rev. A **60**, 2822 (1999).

[50] A. Derevianko, W. R. Johnson, M. S. Safronova, and J. F. Babb, High-Precision Calculations of Dispersion Coefficients, Static Dipole Polarizabilities, and Atom-Wall Interaction Constants for Alkali-Metal Atoms, Phys. Rev. Lett. **82**, 3589 (1999).

[51] S. Magnier and M. Aubert-Frécon, Static dipolar polarizabilities for various electronic states of alkali atoms, J. Quantum Spectrosc. Radiat. Transf. **75**, 121 (2002).

[52] J. Mitroy and M. W. J. Bromley, Semiempirical calculation of van der Waals coefficients for alkali-metal and alkaline-earth-metal atoms, Phys. Rev. A **68**, 052714 (2003).

[53] M. S. Safronova and C. W. Clark, Inconsistencies between lifetime and polarizability measurements in Cs, Phys. Rev. A **69**, 040501 (2004).

[54] I. S. Lim, P. Schwerdtfeger, B. Metz, and H. Stoll, All-electron and relativistic pseudopotential studies for the group 1 element polarizabilities from K to element 119, J. Chem. Phys. **122**, 104103 (2005).

[55] E. Iskrenova-Tchoukova, M. S. Safronova, and U. I. Safronova, High-precision study of Cs polarizabilities, J. Comput. Methods Sci. Eng. **7**, 521 (2007).

[56] U. I. Safronova and M. S. Safronova, High-accuracy calculation of energies, lifetimes, hyperfine constants, multipole polariz-abilities, and blackbody radiation shift in ^{39}K, Phys. Rev. A **78**, 052504 (2008).

[57] M. S. Safronova and U. I. Safronova, Critically evaluated the-oretical energies, lifetimes, hyperfine constants, and multipole polarizabilities in ^{87}Rb, Phys. Rev. A **83**, 052508 (2011).

[58] D. K. Nandy, Y. Singh, B. P. Shah, and B. K. Sahoo, Transition properties of a potassium atom, Phys. Rev. A **86**, 052517 (2012).

[59] A. Borschevsky, V. Pershina, E. Eliav, and U. Kaldor, *Ab initio* studies of atomic properties and experimental behavior of element 119 and its lighter homologs, J. Chem. Phys. **138**, 124302 (2013).

[60] M. S. Safronova, U. I. Safronova, and C. W. Clark, Magic wavelengths for optical cooling and trapping of potassium, Phys. Rev. A **87**, 052504 (2013).

[61] B. K. Sahoo and B. Arora, Magic wavelengths for trapping the alkali-metal atoms with circularly polarized light, Phys. Rev. A **87**, 023402 (2013).

[62] J. Jiang, L. Y. Tang, and J. Mitroy, Tune-out wavelengths for potassium, Phys. Rev. A **87**, 032518 (2013).

[63] T. Yong-Bo, L. Cheng-Bin, and Q. Hao-Xue, Calculations on polarization properties of alkali metal atoms using Dirac-Fock plus core polarization method, Chin. Phys. B **23**, 063101 (2014).

[64] L. Young, W. T. Hill, S. J. Sibener, S. D. Price, C. E. Tanner, C. E. Wieman, and S. R. Leone, Precision lifetime measurements of Cs $6p^2 P_{1/2}$ and $6p^2 P_{3/2}$ levels by single-photon counting, Phys. Rev. A **50**, 2174 (1994).

[65] U. Volz and H. Schmoranzer, Precision lifetime measurements on alkali atoms and on helium by beam–gas–laser spectroscopy, Phys. Scr. **T65**, 48 (1996).

[66] H. Wang, J. Li, X. T. Wang, C. J. Williams, P. L. Gould, and W. C. Stwalley, Precise determination of the dipole matrix element and radiative lifetime of the ^{39}K 4p state by photoasso-ciative spectroscopy, Phys. Rev. A **55**, R1569 (1997).

[67] H. Wang, P. L. Gould, and W. C. Stwalley, Long-range inter-action of the ^{39}K(4s)+^{39}K(4p) asymptote by photoassociative spectroscopy. I. The 0_g^i pure long-range state and the long-range potential constants, J. Chem. Phys. **106**, 7899 (1997).

[68] J. E. Simsarian, L. A. Orozco, G. D. Sprouse, and W. Z. Zhao, Lifetime measurements of the 7p levels of atomic francium, Phys. Rev. A **57**, 2448 (1998).

[69] R. J. Rafac, C. E. Tanner, A. E. Livingston, and H. G. Berry, Fast-beam laser lifetime measurements of the cesium 6p $^2 P_{1/2,3/2}$ states, Phys. Rev. A **60**, 3648 (1999).

[70] S. Falke, I. Sherstov, E. Tiemann, and C. Lisdat, The $A^1\Sigma_u^+$ state of K_2 up to the dissociation limit, J. Chem. Phys. **125**, 224303 (2006).

[71] C. Amiot, O. Dulieu, R. F. Gutterres, and F. Masnou-Seeuws, Determination of the Cs_2 $0_g^-(P_{3/2})$ potential curve and of Cs $6P_{1/2,3/2}$ atomic radiative lifetimes from photoassociation spectroscopy, Phys. Rev. A **66**, 052506 (2002).

[72] N. Bouloufa, A. Crubellier, and O. Dulieu, Reexamination of the 0_g^- pure long-range state of Cs_2: Prediction of missing levels in the photoassociation spectrum, Phys. Rev. A **75**, 052501 (2007).

[73] R. J. Rafac and C. E. Tanner, Measurement of the ratio of the cesium D-line transition strengths, Phys. Rev. A **58**, 1087 (1998).

[74] R. F. Gutterres, C. Amiot, A. Fioretti, C. Gabbanini, M. Mazzoni, and O. Dulieu, Determination of the ^{87}Rb 5p state dipole matrix element and radiative lifetime from the photoassociation spectroscopy of the $Rb_2 0_g^-(P_{3/2})$ long-range state, Phys. Rev. A **66**, 024502 (2002).

[75] C. Gabbanini, A. Fioretti, A. Lucchesini, S. Gozzini, and M. Mazzoni, Cold Rubidium Molecules Formed in a Magneto-Optical Trap, Phys. Rev. Lett. **84**, 2814 (2000).

[76] S. G. Porsev, K. Beloy, and A. Derevianko, Precision determi-nation of weak charge of ^{133}Cs from atomic parity violation, Phys. Rev. D **82**, 036008 (2010).

[77] P. J. Leo, C. J. Williams, and P. S. Julienne, Collision Properties Of Ultracold ^{133}Cs Atoms, Phys. Rev. Lett. **85**, 2721 (2000).

[78] C. Chin, V. Vuletić, A. J. Kerman, S. Chu, E. Tiesinga, P. J. Leo, and C. J. Williams, Precision Feshbach spectroscopy of ultracold Cs_2, Phys. Rev. A **70**, 032701 (2004).

[79] M. S. Safronova, B. Arora, and C. W. Clark, Frequency-dependent polarizabilities of alkali-metal atoms from ultraviolet through infrared spectral regions, Phys. Rev. A **73**, 022505 (2006).

[80] W. F. Holmgren, R. Trubko, I. Hromada, and A. D. Cronin, Measurement of a Wavelength of Light for Which The Energy Shift for an Atom Vanishes, Phys. Rev. Lett. **109**, 243004 (2012).

[81] V. Gerginov, C. E. Tanner, S. A. Diddams, A. Bartels, and L. Hollberg, High-resolution spectroscopy with a femtosecond laser frequency comb, Opt. Lett. **30**, 1734 (2005).

[82] V. Gerginov, K. Calkins, C. E. Tanner, J. J. McFerran, S. Diddams, A. Bartels, and L. Hollberg, Optical frequency measurements of 6s $^2S_{1/2}$ − 6p$^2P_{1/2}$ (D1) transitions in ^{133}Cs and their impact on the fine-structure constant, Phys. Rev. A **73**, 032504 (2006).

[83] S. Falke, E. Tiemann, C. Lisdat, H. Schnatz, and G. Grosche, Transition frequencies of the D lines of ^{39}K, ^{40}K, and ^{41}K measured with a femtosecond laser frequency comb, Phys. Rev. A **74**, 032503 (2006).

[84] I. Johansson, Spectra of the alkali metals in the lead-sulphide region, Ark. Fys. **20**, 135 (1961).

[85] B. M. Patterson, J. F. Sell, T. Ehrenreich, M. A. Gearba, G. M. Brooke, J. Scoville, and R. J. Knize, Lifetime measurement of the cesium 6$P_{3/2}$ level using ultrafast pump-probe laser pulses, Phys. Rev. A **91**, 012506 (2015).

[86] L. R. Hunter, D. Krause, D. J. Berkeland, and M. G. Boshier, Precise measurement of the Stark shift of the cesium D1 line, Phys. Rev. A **44**, 6140 (1991).

[87] K. E. Miller, D. Krause, and L. R. Hunter, Precise measurement of the Stark shift of the rubidium and potassium D1 lines, Phys. Rev. A **49**, 5128 (1994).

[88] A. Derevianko, S. G. Porsev, and J. F. Babb, Electric dipole polarizabilities at imaginary frequencies for hydrogen, the alkali-metal, alkaline-earth, and noble gas atoms, At. Data Nucl. Data Tables **96**, 323 (2010).